DOI: https://doi.org/10.53256/COSE_250102

Directional Decomposition of Experimental Data with Nonlinear Short-Crested Waves Using the NL-SORS Method

S. K. Iversen[a,*], T. Lykke Andersen[a], F. Alfaro Corrales[b] and M. R. Eldrup[a]
[a]*Department of the Built Environment, Aalborg University, Aalborg, Denmark*
[b]*Department of Civil Engineering, Ghent University, Ghent, Belgium*

[*]*Corresponding author: Sarah Krogh Iversen (ski@build.aau.dk)*

ABSTRACT: In physical model testing of coastal structures, the wave conditions acting on the structure are typically assessed from surface elevation measurements, which provide the total sea-surface elevation of the generated sea state. However, to relate structural loading and response to the incident wave field, it is necessary to estimate the incident wave components separately. The NL-SORS method for separation of incident and reflected nonlinear short-crested waves, based on measurements from a wave gauge array, has recently been introduced and validated using synthetic data. In the present study, the method is applied to experimental data covering a range of directional spreading conditions and levels of nonlinearity. For all tested cases, the method demonstrates stability and successfully reconstructs both the decomposed surface elevation time series and the corresponding three-dimensional directional wave spectrum.

KEYWORDS: Wave Analysis, Multidirectional Waves, Incident Waves, Wave Separation, Physical Modelling

1 INTRODUCTION

In physical model testing of coastal structures, it is essential to determine the incident waves acting on the structure. In the absence of a structure, incident waves may be measured using a single wave gauge, provided that passive absorption is sufficiently effective. However, for short-crested waves, a single gauge does not provide information on the directional spectrum. When a structure is present, multiple gauges or co-located wave gauges are required to estimate the incident waves by applying wave separation techniques.

Traditional separation methods for long-crested (2D) waves, based on surface elevation measurements at multiple locations, were introduced by Goda and Suzuki (1976) for two wave gauges and by Mansard and Funke (1980) for three wave gauges. These methods were later extended by Zelt and Skjelbreia (1993) to accommodate an arbitrary number of wave gauges. In these approaches, the incident and reflected components are separated based on phase differences between measurement locations.

For nonlinear long-crested waves, the system of equations was extended to include bound nonlinear components by Lin and Huang (2004) for regular waves, while Lykke Andersen et al. (2017) incorporated amplitude dispersion effects. Eldrup and Lykke Andersen (2019) further extended these principles to irregular waves, and de Ridder et al. (2023) improved their practical implementation. Suh et al. (2001) and Draycott et al. (2019) additionally incorporated current effects into the separation framework.

For short-crested waves, incident wave characteristics can only be estimated using multiple gauges combined with appropriate wave separation methods. Many existing approaches for three-dimensional wave analysis are limited to frequency-domain techniques that provide only the directional wave spectrum and do not enable time-domain separation of the wave field. Examples include the Bayesian Directional Method (BDM) by Hashimoto and Kobune (1988), the Maximum Likelihood Method (MLM) by Capon et al. (1976), Isobe et al. (1984), and Krogstad (1988), as well as the Maximum Entropy Method (MEM) by Hashimoto et al. (1994).

Draycott et al. (2016) proposed exploiting knowledge of the single-summation wave generation method in the directional analysis of linear short-crested waves. Iversen et al. (2024) introduced the SORS method to account for oblique reflections, and Iversen et al. (2025) subsequently extended this framework to nonlinear waves. The NL-SORS method was demonstrated by Iversen et al. (2025) using a limited number of numerical simulations; however, it has not yet been validated using physical model test data. Experimental data may contain additional sources of error that could affect the method's performance.

For the corresponding linear formulation, Iversen et al. (2024) demonstrated low sensitivity to error sources such as additional basin wall reflections, measurement noise, wave gauge misplacement, and calibration errors. However, the inclusion of nonlinear effects—such as bound wave components and simplified amplitude dispersion—leads to a more complex system of equations. Consequently, the nonlinear separation procedure is expected to be more sensitive to noise, measurement inaccuracies, and deviations from the assumed mathematical model than conventional linear methods.

In the present paper, the NL-SORS method proposed by Iversen et al. (2025) is applied to physical model test data. The method is first briefly introduced, followed by a description of the sea states considered in the present analysis. The wave generation procedure is described in detail by Lykke Andersen et al. (2025). The decomposed wave fields are then presented and discussed in relation to the applied wave generation. Finally, the main conclusions are provided.

2 METHODOLOGY

2.1 *Wave Decomposition Using the NL-SORS Method*

The wave decomposition method proposed by Iversen et al. (2025) applies to wave fields generated using the single-summation method and is therefore applicable to both numerical and physical model data produced according to this principle. The method requires a stationary, non-breaking wave field that can be represented as a finite sum of wave components. The incident and reflected wave fields are decomposed using a least-squares approach, minimizing the error between the measured and estimated signals in the frequency domain.

For each Fourier component of the measured surface elevation signals, a mathematical model describes how the observed complex wave amplitudes, $\boldsymbol{\zeta}$, are related to the phase-difference matrix, $\boldsymbol{C}$, and the complex amplitudes of the separated wave components, $\boldsymbol{X}$, through the linear system of equations given in Eq. (1).

$$\boldsymbol{CX} = \boldsymbol{\zeta} \tag{1}$$

The phase-difference matrix $\boldsymbol{C}$ contains information on the wave celerity, the direction of propagation of the wave components at the given frequency, and the spatial positions of the measurement points. In traditional linear two-dimensional (2D) wave separation methods, the phase-difference matrix is constructed using linear dispersion theory and by assuming that reflected waves propagate in the opposite direction to incident waves, as wave propagation is restricted to the x-direction.

For linear three-dimensional (3D) separation techniques based on the single-summation assumption, the system of equations is fundamentally similar. However, instead of restricting the reflected waves to propagate in the opposite direction of the incident waves, the direction of propagation of each separated wave component is estimated by fitting the model to the observed Fourier components using a least-squares procedure, as in the traditional 2D methods. Under the single-summation assumption, each frequency component is assumed to have only one incident direction. Estimation of the propagation directions requires a non-collinear wave gauge array with an appropriate geometric configuration, as discussed by Iversen et al. (2025).

For nonlinear separation techniques in both 2D and 3D, the system of equations is extended to include bound nonlinear components, and simplified amplitude dispersion is introduced for the identified subharmonic, primary, and superharmonic frequency regions. As the number of unknown components increases, the number of wave gauges required for a robust decomposition must also increase accordingly.

When applying the NL-SORS method (Iversen et al., 2025), it is assumed that, for each frequency component in the nonlinear regions, the analysed 3D wave field can be represented by a maximum of four components: an incident free, incident bound, reflected free, and reflected bound component. The validity of this assumption was examined in detail by Iversen et al. (2025). Each component may have its own propagation direction, θ, which effectively determines whether it is classified as incident or reflected. The celerity of the bound components is defined based on a narrowband assumption of both the frequency spectrum and the directional spreading function. The system of equations for a total of

$$\begin{bmatrix} e^{\mathrm{i}\omega \boldsymbol{k}_{I,F}^{(n)}(\theta_{I,F}^{(n)})\boldsymbol{x}_1} & e^{\mathrm{i}\omega \boldsymbol{k}_{I,B}^{(n)}(\theta_{I,B}^{(n)})\boldsymbol{x}_1} & e^{\mathrm{i}\omega \boldsymbol{k}_{R,F}^{(n)}(\theta_{R,F}^{(n)})\boldsymbol{x}_1} & e^{\mathrm{i}\omega \boldsymbol{k}_{R,B}^{(n)}(\theta_{R,B}^{(n)})\boldsymbol{x}_1} \\ e^{\mathrm{i}\omega \boldsymbol{k}_{I,F}^{(n)}(\theta_{I,F}^{(n)})\boldsymbol{x}_2} & \vdots & \vdots & \vdots \\ \vdots & \vdots & \vdots & \vdots \\ e^{\mathrm{i}\omega \boldsymbol{k}_{I,F}^{(n)}(\theta_{I,F}^{(n)})\boldsymbol{x}_M} & e^{\mathrm{i}\omega \boldsymbol{k}_{I,B}^{(n)}(\theta_{I,B}^{(n)})\boldsymbol{x}_M} & e^{\mathrm{i}\omega \boldsymbol{k}_{R,F}^{(n)}(\theta_{R,F}^{(n)})\boldsymbol{x}_M} & e^{\mathrm{i}\omega \boldsymbol{k}_{R,B}^{(n)}(\theta_{R,B}^{(n)})\boldsymbol{x}_M} \end{bmatrix} \begin{bmatrix} X_{I,F} \\ X_{I,B} \\ X_{R,F} \\ X_{R,B} \end{bmatrix} = \begin{bmatrix} \hat{\eta}(\boldsymbol{x}_1) \\ \hat{\eta}(\boldsymbol{x}_2) \\ \vdots \\ \hat{\eta}(\boldsymbol{x}_M) \end{bmatrix} \quad (2)$$

M gauge positions is expressed in matrix form as given in Eq. (2).

The superscript (n) denotes the frequency region (subharmonic, primary, or superharmonic) to which the component belongs. The subscripts I and R refer to incident and reflected components, respectively, while F and B denote free and bound components.

In the primary region, the system reduces to two components, as only primary (free) waves are assumed to be present. In the subharmonic and superharmonic regions, the number of components is reduced only if the condition number of the system exceeds a prescribed threshold, as suggested by de Ridder et al. (2023).

The output of the NL-SORS analysis consists of the decomposed complex wave amplitudes, $\boldsymbol{X}$, together with the corresponding propagation directions, θ, of each component. Based on their directions, the components are classified as incident or reflected. From the decomposed components, the 3D directional spectrum can be reconstructed following the procedure described by Draycott et al. (2015). Furthermore, the surface elevation of the separated wave fields can be reconstructed at arbitrary spatial locations, enabling direct correlation between structural response and the incident wave field.

2.2 Ad Hoc Unified Wave Generation

In the present study, waves in the physical model are generated using the ad hoc unified wave generation method proposed by Zhang et al. (2007). This approach requires depth-averaged particle velocities as input, which, in the present tests, are obtained from the numerical model Celeris (Tavakkol and Lynett, 2017). In the numerical model, short-crested waves are generated in deeper water at a water depth h_{deep} using the single-summation method. The waves are subsequently propagated over a gently sloping seabed with a slope of 1:80. The depth h_{deep} is selected such that second-order wave theory remains valid for wave generation within the numerical domain. The physical model represents a subsection of the full numerical domain, as illustrated in Figure 1.

In the region corresponding to the physical model domain, the seabed is horizontal, and the water depth is denoted by h.

The coupled numerical–physical modelling approach enables the generation of highly nonlinear waves in the physical model without the need for transition slopes or the application of wavemaker theories outside their validity range. Both of these alternatives may introduce spurious free-wave components, as demonstrated by Eldrup and Lykke Andersen (2024). Further details regarding the numerical model setup and discretisation are provided by Lykke Andersen et al. (2025).

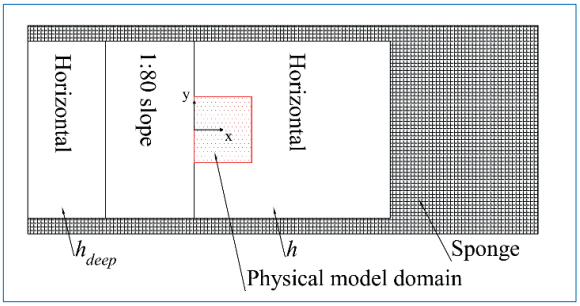

Figure 1. Plan v view of the numerical model setup (not to scale). The mean wave propagation direction is from left to right. Waves in the numerical model are generated along the left boundary.

2.3 Physical Model Setup

The physical model tests were conducted at the Ocean and Coastal Engineering Laboratory at Aalborg University, Denmark. The wave basin has an active area of 13 × 8.4 m and is equipped with 30 vertically hinged, individually controlled piston-type wavemakers, enabling accurate generation of three-dimensional (3D) wave fields. Efficient passive absorption is installed along the rear wall and parts of the sidewalls. The experiments were performed over a horizontal seabed and without any structure present. Consequently, wave reflections are expected to be limited and predominantly linear. The wave field was analysed based on surface elevation measurements obtained from an array of wave gauges, as shown in Figure 2.

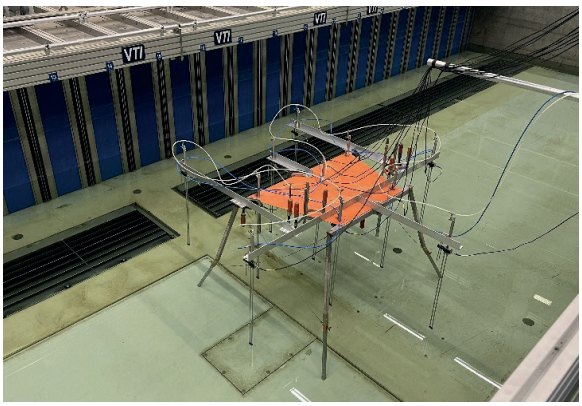

Figure 2. Physical model setup in the wave basin at the Ocean and Coastal Engineering Laboratory, Aalborg University.

The same wave gauge array was used for all tested sea states in the present analysis. The layout of the array and its position within the basin are shown in Figure 3.

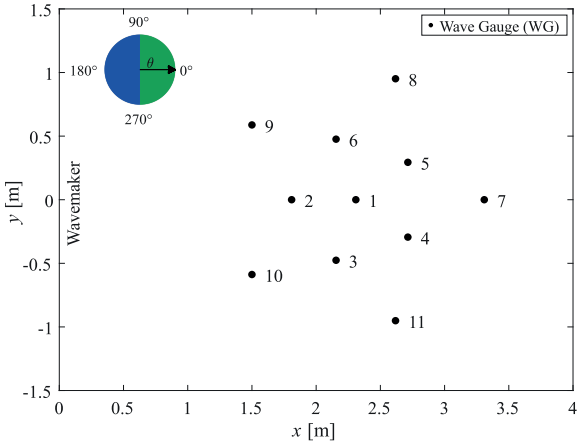

Figure 3. Wave gauge array configuration. Wave gauge 1 is located at the centre of the array. Wave gauges 2–6 are evenly distributed along an inner circle with diameter $D_1 = 1$m. Wave gauges 7–11 are evenly distributed along an outer circle with diameter $D_2 = 2$m. Incident (green) and reflected (blue) wave propagation directions (θ) are indicated.

The basin coordinate system is defined such that the basin centreline coincides with the x-axis (see Figure 1). The wave propagation direction, θ, is defined such that θ = 0° corresponds to the positive x-direction, with positive angles measured counterclockwise.

The waves were generated without corner reflection control. As a result, diffraction and reflection zones are expected near the sidewalls of the basin (cf. Dalrymple, 1989). The wave gauge array was therefore positioned such that the innermost gauges were located just outside the nearfield region, which was conservatively defined as three water depths from the mean wavemaker position.

2.4 *Input Sea States*

To evaluate the performance of the decomposition method using physical model data, several multidirectional, nonlinear sea states were tested. The waves were generated using a $\cos^{2s}$ directional spreading function. The test programme included two sea states (Tests 00–01) characterised by broad directional spreading, defined by a small spreading parameter $s = 15$, and four sea states (Tests 02–05) with narrower directional spreading ($s = 50$) and progressively decreasing wave steepness. All sea states were generated in the numerical model at a water depth h_{deep}. The frequency spectrum in all cases followed a JONSWAP distribution with a peak enhancement factor $\gamma = 3.3$. In the physical model, the water depth was constant at $h = 0.5$m, with a horizontal seabed. The wave gauge array configuration was identical to that used by Iversen et al. (2025). Because the same array layout was applied to all tests, the ratios between the array diameters and the wavelength at the spectral peak frequency, L_p, are also reported. Iversen et al. (2025) recommended diameter-to-wavelength ratios of 0.15 and 0.30 for optimal performance. The input parameters for the sea states generated in the numerical model are summarised in Table 1.

Table 1: Numerical model input parameters: spectral significant wave height at the physical model wavemaker (H_{m0}); peak period (T_p); mean wave direction (θ_0); directional spreading parameter (s); peak enhancement factor (γ); water depth in the deep region of the numerical model (h_{deep}); water depth in the physical model domain (h); and ratios between the inner (D_1/L_p) and outer (D_2/L_p) diameters of the wave gauge array and the wavelength at the spectral peak frequency (L_p).

ID	H_{m0} [m]	T_p [s]	θ_0 [°]	s [-]	γ [-]	h_{deep} [m]	h [m]	D_1/L_p [-]	D_2/L_p [-]
Test00	0.15	2.5	0	15	3.3	0.635	0.5	0.19	0.38
Test01	0.15	3.0	0	15	3.3	0.756	0.5	0.16	0.31
Test02	0.15	2.5	0	50	3.3	0.746	0.5	0.19	0.39
Test03	0.15	3.0	0	50	3.3	0.746	0.5	0.16	0.31
Test04	0.15	3.5	0	50	3.3	0.859	0.5	0.13	0.26
Test05	0.15	4.0	0	50	3.3	0.972	0.5	0.12	0.23

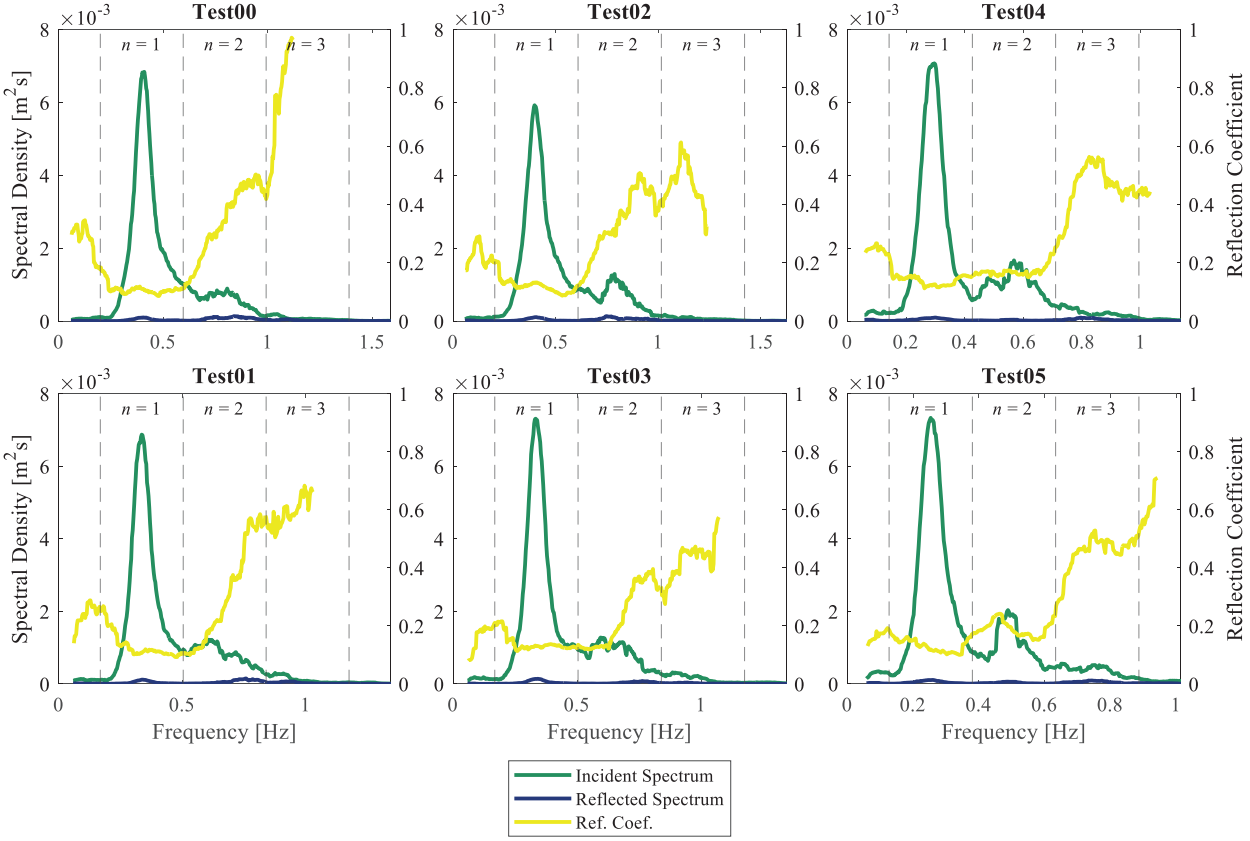

Figure 4. Estimated incident and reflected wave spectra obtained using the NL-SORS method. The left vertical axis represents the spectral density of the decomposed spectra, while the right vertical axis shows the estimated reflection coefficient, calculated as the ratio of reflected amplitude to incident amplitude.

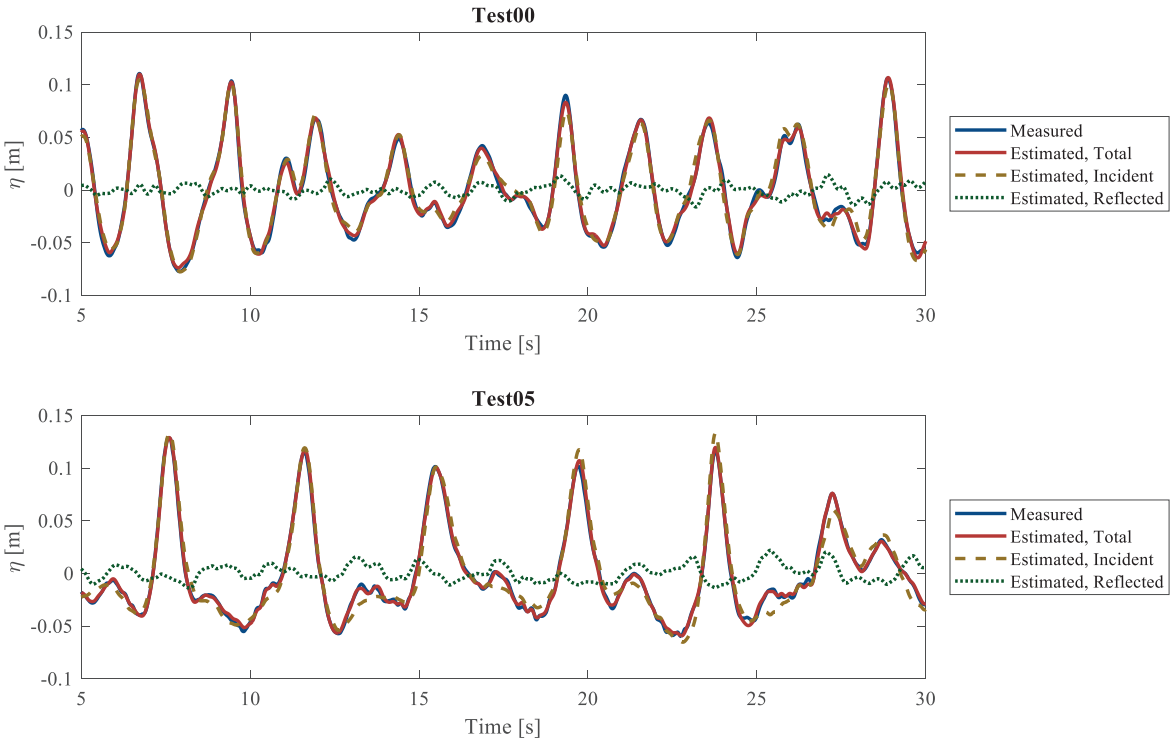

Figure 5. Comparison between estimated and measured surface elevation time series at the location of wave gauge 1 for the most directionally spread sea state, Test00 (top), and the most nonlinear sea state, Test05 (bottom). For both cases, the selected time window contains the largest wave recorded during the test duration.

3 RESULTS

The results obtained using the NL-SORS method are presented below. During the physical model tests, no wave breaking was observed. The surface elevation signals revealed a difference in energy levels at WG7 (cf. Figure 3), which may be attributed to diffraction effects within the basin, as WG7 is located furthest from the wavemakers. Since diffraction effects are not accounted for in the applied method, WG7 was excluded from the analysis.

The resulting decomposed wave spectra are shown in Figure 4. The method estimates a low level of reflections in the physical wave basin. In the primary frequency region, the reflection coefficient is approximately 0.12, which is consistent with the expected performance of the passive absorption system. Reflections increase at higher frequencies, which is also anticipated given the characteristics of the passive absorption system composed of vertical layers of expanded metal sheets.

The reconstruction of the surface elevation time series is illustrated in Figure 5 for Test00 and Test05 at the position of wave gauge 1, located at the centre of the array. Test00 represents the most directionally spread and least nonlinear sea state analysed, whereas Test05 is the least directionally spread but most nonlinear case. For Test05, nonlinear features characterised by high, narrow crests and broader, shallower troughs are successfully reproduced by the NL-SORS method. The results demonstrate that, even under conditions of high directional spreading and strong nonlinearity, the reconstructed total surface elevation at the array centre closely matches the measured signal.

A comparison between the reconstructed and measured total surface elevations for all tests is shown in Figure 6. Results obtained using the linear SORS method (Iversen et al., 2024) and the linear SPAIR method (Draycott et al., 2016) are included to highlight the importance of incorporating nonlinear contributions. The reconstruction error is quantified using the relative variance error, averaged over all gauge positions, as summarised in Table 2.

Table 2: Relative variance error of the reconstructed total surface elevation compared with measured signals (mean value over all gauge positions).

ID		SPAIR	SORS	NL-SORS
Test00	C1	4.17%	4.77 %	1.33%
Test01	D1	3.11%	3.15 %	0.83%
Test02	C2	3.41%	2.78 %	0.90%
Test03	D2	2.38%	1.99 %	0.64%
Test04	E2	2.00%	1.57 %	0.43%
Test05	F2	1.84%	1.33 %	0.33%

Based on the variance errors, the reconstruction accuracy improves as directional spreading decreases, as observed when comparing Test00 with Test02 and Test01 with Test03. Furthermore, accuracy improves progressively from Test02 to Test05. This trend may partly result from reduced directional spreading and increased nonlinear transformation during propagation over the numerical model slope. As the slope length increases across these cases, nonlinear waves undergo stronger refraction, which may enhance the consistency of the directional structure within the array.

Additionally, the estimated wave directions influence the spatial variability of surface elevation within the fixed-size array. For longer waves, the relative variation across the array is smaller than for shorter waves. Therefore, the ratio between array dimensions and the peak wavelength should be considered when evaluating method performance. From Test02 to Test05, the peak wavelength increases, reducing the relative distance between the array centre and its outer diameter. Iversen et al. (2025) demonstrated that reconstruction accuracy decreases with increasing distance from the array centre.

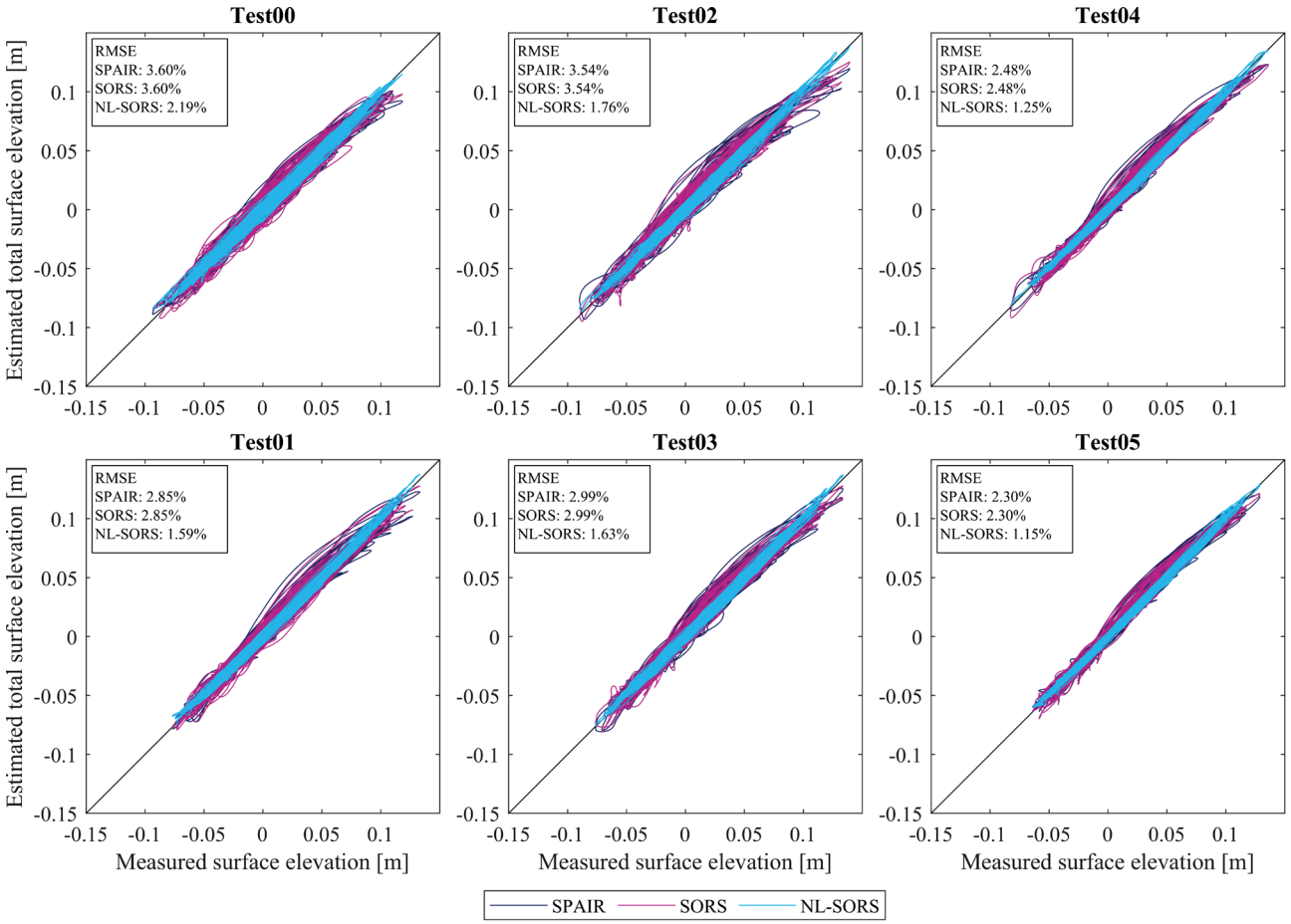

Figure 6. Comparison of the reconstructed total surface elevation and the measured surface elevation at wave gauge position 1 (see Figure 3). A perfect agreement corresponds to the diagonal line. The root-mean-square error (RMSE) is reported relative to the significant wave height.

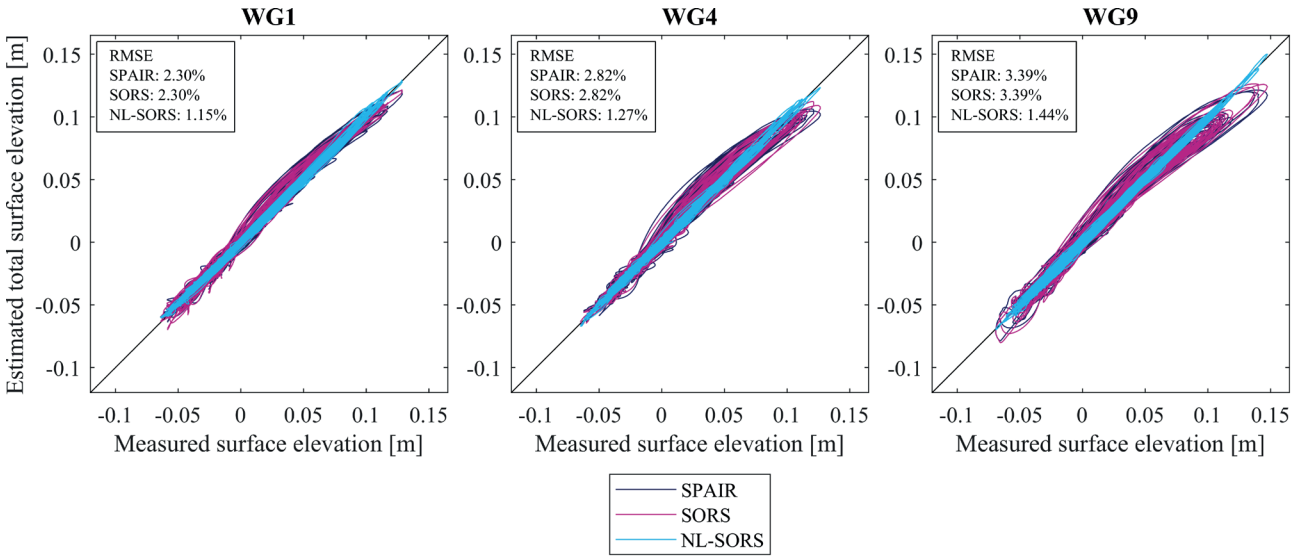

Figure 7. Comparison of the reconstructed and measured total surface elevation for Test05 at three wave gauge locations with increasing distance from the array centre: WG1 (0 m), WG4 (1 m), and WG9 (2 m). A perfect agreement corresponds to the diagonal line.

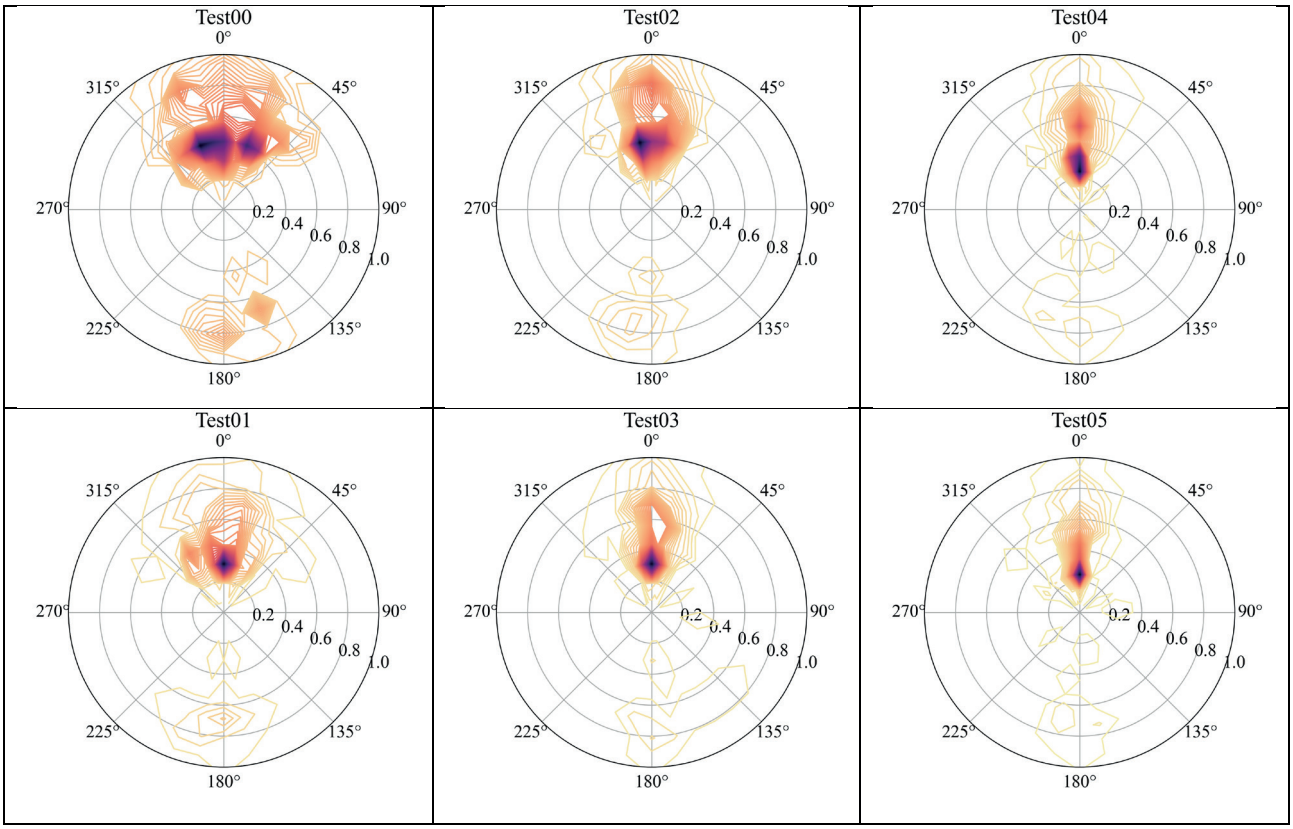

Figure 8. Reconstructed three-dimensional directional spectra obtained using the NL-SORS method. Spectral density is represented by the colour scale of the contour plot, ranging from light yellow/orange (lowest spectral density) to dark purple/blue (highest spectral density). The radial coordinate represents frequency (Hz).

This effect becomes more pronounced for highly nonlinear cases, as uncertainties in the mathematical model primarily relate to the celerity and direction of higher-order bound components. These bound components have lower amplitudes in less nonlinear cases, consistent with the estimated spectra shown in Figure 4. To ensure accurate reconstruction over a larger spatial area, inclusion of nonlinear effects is essential. This conclusion is supported by the present analyses, as illustrated in Figure 7, which compares reconstructed total surface elevations for Test05 at the centre, inner diameter, and outer diameter of the wave gauge array.

In addition to decomposed spectra and reconstructed surface elevation time series, the NL-SORS method enables reconstruction of the estimated three-dimensional directional spectrum (Figure 8). The decomposed wave components are grouped into 36 directional bins and 512 frequency bins, corresponding to averaging over 32 wave components in the frequency domain. The resulting directional spectra confirm that incident and reflected wave directions are identified correctly, and they show that directional spreading decreases with increasing peak wave period.

4 DISCUSSION

To further evaluate the performance of the method, the decomposition into free and bound wave components is examined. For Test03, Figure 9 shows a pronounced peak in the spectral density of the bound incident spectrum in the second-order superharmonic region (n = 2), as well as a smaller peak in the third-order superharmonic region (n = 3). This behaviour is expected given the nonlinearity of the sea state. The free (primary) component of the spectrum closely resembles a JONSWAP distribution.

For the most nonlinear sea state, Test05, the increase in energy within the second-order region is even more pronounced (see Figure 4). However, Figure 10 indicates that a larger proportion of superharmonic free energy is estimated, and the spectral shape deviates from the expected JONSWAP form. Since this deviation is most evident for the sea state with the smallest directional spreading, it is unlikely to be caused by the narrow-banded directional spreading assumption of the present method, which should in fact perform more accurately for longer waves (cf. Iversen et al., 2025). Instead, the elevated level of free energy may be related either to limitations in the separation method or to characteristics of the physical wave generation.

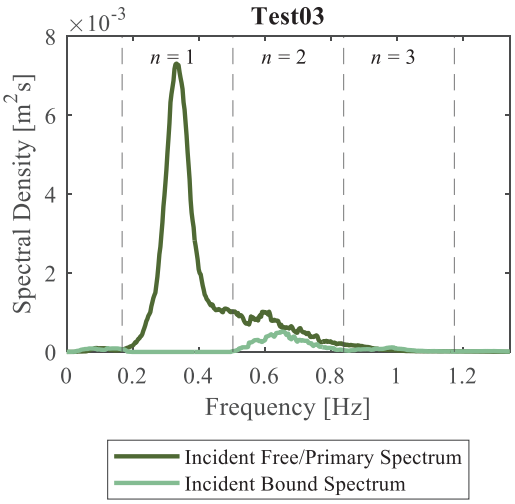

Figure 9. Estimated incident spectrum for Test03 using the NL-SORS method, separated into free (primary) and bound components.

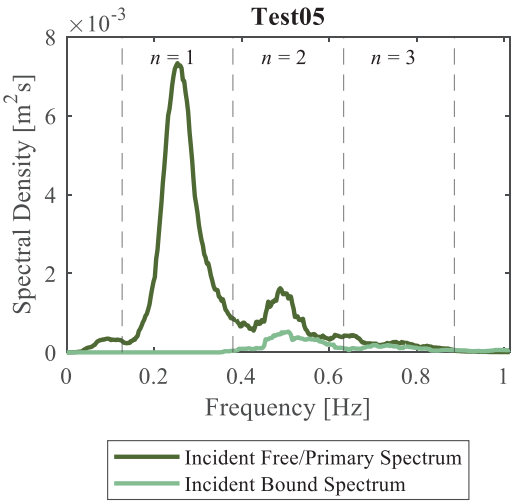

Figure 10. Estimated incident spectrum for Test05 using the NL-SORS method, separated into free (primary) and bound components.

In relation to the separation method, Eldrup and Lykke Andersen (2019) demonstrated that if the celerities of the free and bound components are nearly identical, accurate separation is not possible. This condition may be assessed using Eq. (3) for the *i*th frequency component:

$$\frac{c_B}{c_F} = \frac{k_i}{n \cdot k_i(\omega/n)} > \alpha \qquad (3)$$

Eldrup and Lykke Andersen (2019) suggested a conservative threshold value of α = 1.15, while values in the range 1.05–1.15 may occasionally yield reliable results. The ratios between bound and free celerities in the second-order superharmonic region for the present test cases are summarised in Table 3.

Table 3: Ratio between bound and free wave celerity in the second-order superharmonic region (evaluated at $2f_p$).

ID	c_B/c_F
Test00	1.20
Test01	1.13
Test02	1.21
Test03	1.13
Test04	1.09
Test05	1.07

A key distinction between the present NL-SORS method and the two-dimensional application described by Eldrup and Lykke Andersen (2019) is that, in NL-SORS, bound and free components may propagate in different directions, even when both are incident. However, since Test05 was generated with limited directional spreading and experienced significant refraction, the free and bound components may not differ sufficiently in direction or celerity to allow robust separation. In such cases, the allocation between free and bound components may become ambiguous. As shown in Table 3, the celerity ratios approach unity with increasing nonlinearity, which may explain the elevated level of free energy observed for Test05 in Figure 10.

The increased free energy may also be attributed to the physical wave generation. As shown in Figures 11 and 12, the primary spectral energy from the numerical model is not fully reproduced in the physical model for Test05, whereas the agreement is stronger for Test03. This discrepancy may result from energy losses, for example due to leakage beneath and between wavemaker paddles. Consequently, the primary waves in the physical model for Test05 may bind less energy than predicted numerically. As a result, part of the bound energy in the higher-order regions may be released as free waves. The reduction in primary spectral density is not due to wave breaking, as no breaking was observed during the experiments.

The validity of the numerical model should also be considered. If the numerical simulation overestimates the amount of bound energy relative to what can physically be sustained in the basin, excess energy may similarly be released as free components. Furthermore, incomplete absorption of reflections from the basin walls may result in re-reflection at the paddles, causing additional free components within the directional range defined as incident.

Overall, multiple physical mechanisms may influence the observed wave field. It is therefore not possible to conclusively determine whether the elevated free energy in the second-order region arises from limitations of the separation method or from the characteristics of the physical wave generation. Nevertheless, despite potential ambiguities in the free–bound separation, the reconstructed incident time series and spectra appear robust and physically consistent.

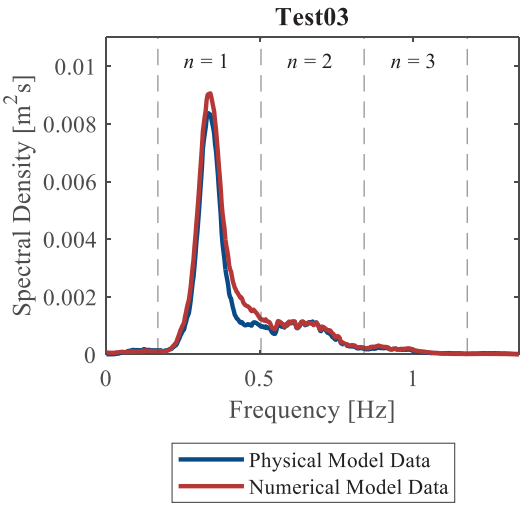

Figure 11. Average measured spectral density for physical and numerical model data, Test03. The average is computed across all gauge positions shown in Figure 3.

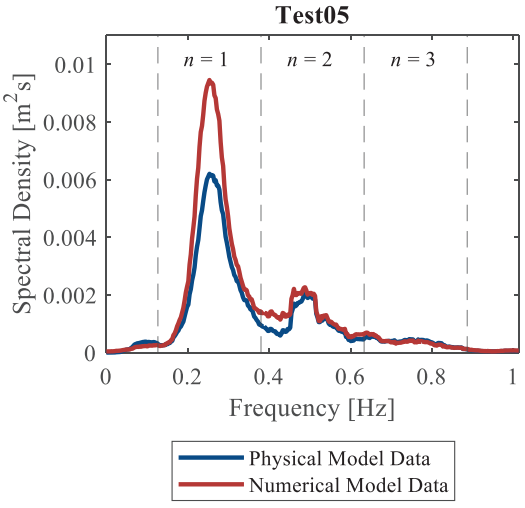

Figure 12. Average measured spectral density for physical and numerical model data, Test05. The average is computed across all gauge positions shown in Figure 3.

5 CONCLUSIONS

A method for the directional separation of nonlinear, short-crested waves generated using the single-summation method was presented by Iversen et al. (2025), who demonstrated its performance using synthetic data from a numerical model. In the present study, the method has been evaluated using experimental data obtained from physical model tests conducted in the wave basin of the Ocean and Coastal

Engineering Laboratory at Aalborg University. The waves were generated using ad hoc unified wave generation, whereby the wavemakers were driven by results from numerical simulations of waves propagating over a mild slope. Two sea states with large directional spreading and four sea states with smaller directional spreading and increasing nonlinearity were investigated.

For the longest and most nonlinear test case, results indicate that, in the second-order superharmonic region, free energy may either be physically released or inaccurately estimated by the separation method. Such discrepancies may arise because the celerities of the free and bound components are nearly identical, which limits the ability of the method to distinguish between them. The applied wave generation technique and the performance of the basin's absorption system require further evaluation before definitive conclusions can be drawn regarding the capability of the method to reliably separate free and bound components in highly nonlinear sea states.

Based on the present analysis, it is concluded that the NL-SORS method is stable when applied to experimental data and that the reconstructed surface elevation time series exhibit high accuracy for all tested sea states within the spatial extent of the wave gauge array.

ACKNOWLEDGEMENTS

This work was supported by the Danish Energy Agency under the Energy Technology Development and Demonstration Program (EUDP), contract number 64022-1062, Niels Bohrs Vej 8D, 6700 Esbjerg, Denmark.

REFERENCES

Capon, J., Greenfield, R.J., Kolker, R.J. (1976). Multidimensional maximum-likelihood processing of a large aperture seismic array. *Proc. IEEE 55*, 192–211.

Dalrymple, R.A. (1989). Directional wavemaker theory with sidewall reflection. *Journal of Hydraulic Research*, 27, 1, 23-34.

Draycott, S., Davey, T., Ingram, D.M., Lawrence, J., Day, A., Johanning, L. (2015). Using a phase-time-path-difference approach to measure directional wave spectra in Flowave. *EWTEC Conference Proceedings*.

Draycott, S., Davey, T., Ingram, D.M., Day, A., Johanning, L. (2016). The SPAIR method: Isolating incident and reflected directional wave spectra in multidirectional wave basins. *Coastal Engineering 114*, 265–283.

Draycott, S., Pillai, A.C., Ingram, D.M., Johanning, L. (2019). Resolving combined wave-current fields from measurements using interior point optimization. *Coastal Engineering*.

Eldrup, M.R., Lykke Andersen, T. (2019). Estimation of incident and reflected wave trains in highly nonlinear two-dimensional irregular waves. *Journal of Waterway, Port, Coastal and Ocean Engineering 145(1)*.

Eldrup, M. R. and Lykke Andersen, T. (2024). Generation of Highly Nonlinear Waves in a Short Wave Flume. *CoastLab24, Delft, The Netherlands.*

Goda, Suzuki (1976). Estimation of incident and reflected waves in random wave experiments. *Proceedings of the 15th Coastal Engineering Conference*, 828‑845.

Hashimoto, N., Kobune, K. (1988). Directional spectrum estimation from a bayesian approach. *Coastal Engineering Proceedings 1(21),4*, 62‑76.

Hashimoto, N., Nagai, T., Asai, T. (1994). Extension of the maximum entropy principle method for directional wave spectrum estimation. *Proceedings of 24th International Conference on Coastal Engineering, Kobe, Japan*, 232–246.

Isobe, M., Kondo, K., Horikawa, K. (1984). Extension of mlm for estimating directional wave spectrum. Proc. Sympo. *On Description and Modelling of Directional Seas A-6.*

Iversen, S.K., Andersen, T.L., Frigaard, P. (2024). Directional spectrum estimation for sea states generated by the single summation method. *Journal of Coastal and Hydraulic Structures 4, 36*.

Iversen, S. K., Eldrup, M. R., Lykke Andersen, T., Frigaard, P. (2025). The NL-SORS Method for Separation of Nonlinear Multidirectional Waves into Incident and Reflected Wave Trains. *Coastal Engineering*.

Krogstad, H.E. (1988). Maximum likelihood estimation of ocean wave spectra from general arrays of wave gauges. *Modelling, Identification and Control 9*, 373–381.

Lin, C.Y., Huang, C.J. (2004). Decomposition of incident and reflected higher harmonic waves using four wave gauges. *Coastal Engineering 51*, 395‑406.

Lykke Andersen, T., Eldrup, M.R., Frigaard, P. (2017). Estimation of incident and reflected components in highly nonlinear regular waves. *Coastal Engineering 119*, 51‑64.

Lykke Andersen, T., Eldrup, M. R., Iversen, S. K. (2025). Recent Advances in Hydraulic Model Testing Techniques. *SCACR 2025.*

Mansard, E.P.D., Funke, E.R. (1980). The measurement of incident and reflected spectra using a least squares method. *Proceedings of the 17th Coastal Engineering Conference*: 154-172.

de Ridder, M.P., Kramer, J., den Bieman, J.P., Wenneker, I. (2023). Validation and practical application of nonlinear wave decomposition methods for irregular waves. *Coastal Engineering 183*.

Suh, K.D., Park, W.S., Park, B.S. (2001). Separation of incident and reflected waves in wave-current flumes. *Coastal Engineering 43*, 149‑159.

Tavakkol, S. and Lynett, P. (2017). Celeris: A GPU-accelerated open source software with a Boussinesq-type wave solver for real-time interactive simulation and visualization. *Computer Physics Communications*, 217, 117-127.

Zelt, J.A., Skjelbreia, J.E. (1993). Estimating incident and reflected wave fields using an arbitrary number of wave gauges. *Coastal Engineering*: 777-789.
Zhang, H., Schäffer, H.A. and Jakobsen, K.P. (2007). Deterministic combination of numerical and physical coastal wave models. *Coastal Engineering*, 54, 171–186.